AIAA JOURNAL
Vol. 31, No. 9, September 1993

Vortical Solutions in Supersonic Corner Flows

R. Marsilio*
Politecnico di Torino, Torino I-10129, Italy

Vortical solutions are investigated for inviscid supersonic steady flows, described by the steady-state Euler equations, that occur in the corner region generated by two orthogonal ramps. Complex shock interactions appear, with the formation of a vorticity field in the corner region and the vorticity itself converging into spiral singularities. Symmetric or asymmetric flow configurations are generated within symmetric corners. The investigation is carried out by a numerical technique based on a space-marching procedure with a finite volume approximation. The integration of the conservation laws allows for the correct numerical capturing of shocks and contact surfaces. A flux-difference-splitting procedure is used for the calculation of the fluxes on the side walls of the volumes, based on the hyperbolicity of the Euler equations for steady supersonic regimes. A high-order accuracy scheme is introduced founded on the essentially nonoscillatory (ENO) scheme. Numerical results are presented and discussed with reference to similar problems investigated by other authors.

Introduction

THIS paper analyzes inviscid, supersonic conical corner flows generated by two intersecting wedges. Such configurations are typical of supersonic inlet flows and are similar to one of the four corners of the box-type inlets. The corner flows are conical if the two intersecting walls are plane. Then all flow variables (pressure, velocity, and entropy) will be independent of the spherical radial coordinate centered at the origin of the corner flow, and these flows will depend only on two space dimensions. Moreover, the topology of a conical flow is characterized by its conical or crossflow streamlines (the projections of the three-dimensional streamlines onto a spherical surface centered at the origin of the flow).

Two possible shock configurations could be generated by the intersection of two compressive wedges. One is characterized by a regular reflection and the other by the presence of a Mach disk (irregular reflection) at the intersection of the two-dimensional shocks produced by each wedge. Such possibilities have been investigated for a symmetrical geometry (two wedges of equal deflection), and the regular reflection shock configuration has been predicted using linearized theory.[1] The Mach disk configuration has been detected experimentally[2] and in the numerical solutions of the Euler equations using a shock-capturing approach[3] and a shock-fitting approach.[4] Figure 1 from Ref. 4 shows in the range of wall deflections (δ) and upstream conditions (M_∞) where the regular or the Mach disk configuration is expected to occur. Note that, for deflections above 5 deg, the only possible solution is the Mach disk shock configuration. Contact surfaces are generated at points where shocks interact because of the different entropies produced by the wave systems on either side of the interaction. However, in the present case of symmetrical geometry and for regular interaction, the strength of the contact surface vanishes. Conversely, in the cases of irregular reflection, two symmetric contact surfaces are generated at the two triple points that bound the Mach disk. For moderate values of upstream Mach number and deflection, the two contact surfaces converge on the corner. According to the results of the present study, when the Mach number or the deflection increases, the configuration may drastically change.

Received June 16, 1992; revision received Nov. 7, 1992; accepted for publication Dec. 4, 1992; presented as Paper 93-0760 at the AIAA 31st Aerospace Sciences Meeting, Reno, NV, Jan. 11-14, 1993.

*Assistant Professor, Department of Aerospace Engineering. Member AIAA.

The numerical procedure for studying these vortical solutions is outlined next. The procedure uses a space-marching upwind formulation based on the flux-difference-splitting (FDS) idea. The Euler equations written as conservation laws are discretized using a finite volume approximation particularly conceived for three-dimensional steady supersonic flows, where the interface values of the fluxes are given by the upwind formulation mentioned earlier. The numerical scheme is of second-order accuracy, with a proper essentially nonoscillatory (ENO) technique to avoid spurious oscillation at flow discontinuities. Computational results are compared with available numerical results of other investigators. Mach number and wall geometry effects are discussed.

Numerical Method

The inviscid steady supersonic conical corner flows are governed by the Euler equations. To provide a numerical procedure capable of a correct numerical capturing of flow discontinuities (shocks and contact surfaces), Euler's equations are written as conservation laws:

$$\int_{\partial \mathrm{Vol}} \rho V \cdot \mathrm{d}S = 0$$

$$\int_{\partial \mathrm{Vol}} \rho V (V \cdot \mathrm{d}S) + \int_{\partial \mathrm{Vol}} p \, \mathrm{d}S = 0 \tag{1}$$

$$\int_{\partial \mathrm{Vol}} (p + e) V \cdot \mathrm{d}S = 0$$

where p, ρ, and e are pressure, density, and total internal energy by unit volume, respectively; V is the velocity vector;

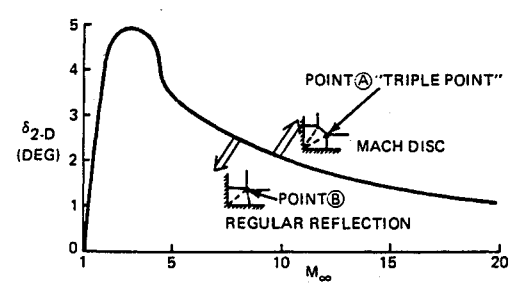

Fig. 1 Maximum deflection for regular reflection (from Ref. 4).

and Vol, ∂Vol, and dS are control volume, boundary surface of the control volume, and the surface element (considered as a vector oriented inward), respectively.

To close the formulation, the state equation of perfect gases, in nondimensional form (all flow variables are nondimensionalized with reference to the upstream conditions),

$$p = \rho T \tag{2}$$

is used, where T is the static temperature of the gas. Moreover, if the total enthalpy of the flow is constant, the energy equation [the last scalar equation in system (1)] may be replaced by the condition

$$V \cdot \nabla h^0 = 0 \tag{3}$$

where h^0 is the total enthalpy of the flow.

The finite volume approach is applied straightforwardly to the integral form of the governing equations (1). A detailed analysis of the procedure is given in Ref. 5. For simplicity, a two-dimensional case is considered in the present analysis. The extension to a three-dimensional problem can be developed easily. Let x and y be two space coordinates and n the unit vector normal to the control surface S, having components n_x and n_y in the x and y directions, respectively. With reference to Fig. 2, Eqs. (1) may be written as

$$\int_{\partial \mathrm{Vol}} w n_x \, \mathrm{d}S + \int_{\partial \mathrm{Vol}} f n_y \, \mathrm{d}S = 0 \tag{4}$$

where

$$w = \begin{pmatrix} \rho u \\ p + \rho u^2 \\ \rho uv \end{pmatrix}, \qquad f = \begin{pmatrix} \rho v \\ \rho uv \\ p + \rho v^2 \end{pmatrix}$$

where u and v are the components of the velocity vector V along x and y, and w and f are the flux vectors in the x and y directions, respectively.

Now, let x be the hyperbolic direction (the flow is supersonic along it), so that it plays the role of the marching direction. Hence, the flux values at x being known, the new values of the flux at $x + \Delta x$ can be evaluated using Eq. (4) and a space-marching technique. The computational domain is divided into quadrilateral cells (volumes), the geometry of which is completely known, as shown in Fig. 3. The computational points of the cell are A and C. Point A is an initial data point, whereas C is the point where the solution has to be computed. With reference to this cell, Eq. (4) is discretized as

$$w_A^k(y_2 - y_1) + w_B^k(y_3 - y_2) + w_C^k(y_4 - y_3) + w_D^k(y_1 - y_4) + f_B^k(x_3 - x_2) + f_D^k(x_1 - x_4) = 0 \tag{5}$$

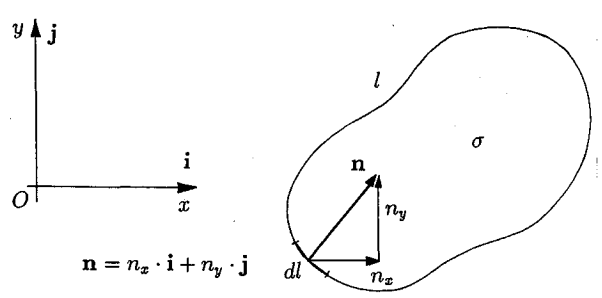

Fig. 2 Two-dimensional control volume.

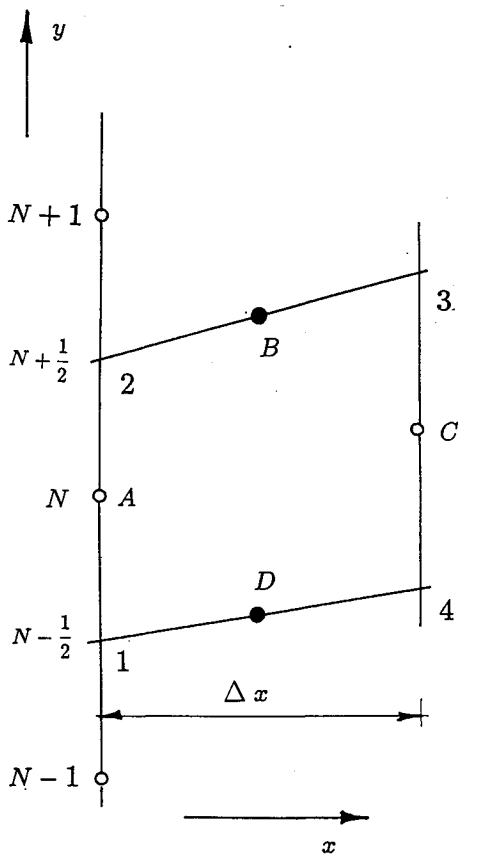

Fig. 3 Two-dimensional finite volume.

where w_j^k and f_j^k are the k flux components ($k = 1, 2, 3$) computed at points j ($j = A, B, C, D$). The flux vectors w and f at the interfaces (points B and D) are evaluated according to the FDS procedure, as shown hereafter. Once the new flux values w_C^k are known, the results are decoded to find the other flow properties, using the energy equation in the form of Eq. (3).

The basic steps of the FDS formulation are the definition and the solution of an appropriate Riemann problem. More details on this formulation conceived for the steady supersonic flows may be found in Ref. 6. Let us focus our attention on point B of Fig. 3. To predict w_B and f_B, a Riemann problem is solved on the basis of the flow properties at points N and $N + 1$, with piecewise constant values distributions, by generating a discontinuity at the interface location $N + ½$, as shown in Fig. 4. The collapse of this discontinuity generates three waves; two acoustic waves and one contact surface. On the basis of the two initially uniform regions (corresponding to N and $N + 1$), two new regions (c, d) are generated. Then the flux at B will be selected as the one of the region in which the side B of the cell is embedded.

Approximate Solver of the Riemann Problem

The Euler equations for the steady supersonic flow are written in the quasilinear form:

$$\kappa P_x + \sigma P_y + \gamma \sigma_y = 0$$

$$\sigma_x + \sigma \sigma_y + (a^2/\gamma u^2)(P_y - \sigma P_x) = 0 \tag{6}$$

$$h_x + \sigma h_y - (a^2/\gamma)(P_x + \sigma P_y) = 0$$

where $\kappa = 1 - a^2/u^2$, and a and γ are the speed of sound and the specific heats ratio, respectively. It is convenient to write the governing equations using the logarithm of pressure ($P = \ln p$), the slope of the streamline ($\sigma = v/u$), and the enthalpy

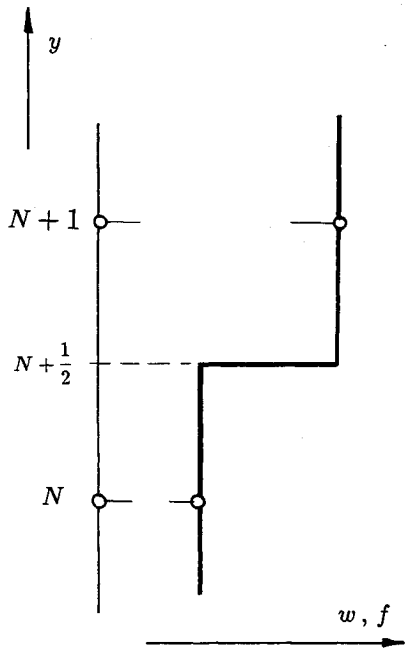

Fig. 4 Definition of the Riemann problem.

h as dependent variables. Owing to their hyperbolic nature, the quasilinear equations may be replaced by the compatibility equations that describe the convection of signals. The collapse of the initial discontinuity shown in Fig. 4 is governed by the compatibility equations. The discontinuity generates a pattern of three waves, labeled *I*, *II*, and *III* in Fig. 5, and the two new uniform regions (c, d) thus generated may be found from the initial ones (a, b) using the compatibility equations (solution of the Riemann problem). Here an approximate solver for the Riemann problem is used, which is shown in a detailed manner in Ref. 6. Namely, the two acoustic waves are considered isentropic whereas through the contact surface the usual conditions (continuity of pressure and streamline direction) are imposed. The slopes of the characteristic lines are defined by Euler's equations as

$$\lambda_1 = \frac{u^2\sigma - a^2\beta}{u^2 - a^2}$$

$$\lambda_2 = \sigma$$

$$\lambda_3 = \frac{u^2\sigma + a^2\beta}{u^2 - a^2}$$

and the signals dR_1, dR_2, and dR_3 that propagate along them, according to the compatability equations, are given by

$$dR_1 = dP - \frac{\gamma u^2}{a^2\beta}\,d\sigma \tag{7}$$

$$dR_2 = dh - \frac{p}{\rho}\,dP \tag{8}$$

$$dR_3 = dP + \frac{\gamma u^2}{a^2\beta}\,d\sigma \tag{9}$$

with $\beta = \sqrt{M^2 - 1}$, where M denotes the Mach number. With reference to Fig. 5, Eqs. (8) and (9) through the *I* wave give

$$P_c + \left(\frac{\gamma u^2}{a^2\beta}\right)_a \sigma_c = R_{3a}$$

$$h_c - \left(\frac{p}{\rho}\right)_a P_c = R_{2a}$$

where

$$R_{3a} = P_a + \left(\frac{\gamma u^2}{a^2\beta}\right)_a \sigma_a$$

$$R_{2a} = h_a - \left(\frac{p}{\rho}\right)_a P_a$$

On the contact surface (wave *II*), continuity of pressure and streamline direction must be imposed:

$$P_c = P_d, \qquad \sigma_c = \sigma_d$$

Finally, the compatability equations [Eqs. (7) and (8)] through the wave *III* give

$$P_d - \left(\frac{\gamma u^2}{a^2\beta}\right)_b \sigma_d = R_{1b}$$

$$h_d - \left(\frac{p}{\rho}\right)_b P_d = R_{2b}$$

where

$$R_{1b} = P_b - \left(\frac{\gamma u^2}{a^2\beta}\right)_b \sigma_b$$

$$R_{2b} = h_b - \left(\frac{p}{\rho}\right)_b P_b$$

The evaluation of the unknowns P, σ, and h in regions c and d proceeds directly from the previous conditions:

$$\sigma_c = \sigma_d = \frac{R_{3a} - R_{1b}}{(\gamma u^2/a^2\beta)_a + (\gamma u^2/a^2\beta)_b}$$

$$P_c = P_d = R_{3a} - \left(\frac{\gamma u^2}{a^2\beta}\right)_a \sigma_c$$

$$h_c = R_{2a} + \left(\frac{p}{\rho}\right)_a P_c, \qquad h_d = R_{2b} + \left(\frac{p}{\rho}\right)_b P_d$$

Having solved the Riemann problem, all flow properties in the two new regions c and d, in particular w and f, follow

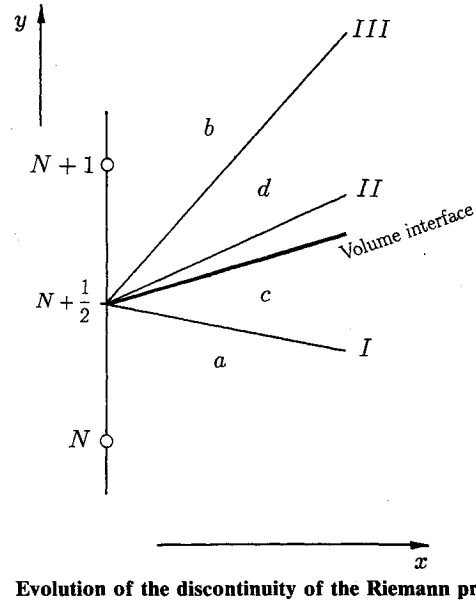

Fig. 5 Evolution of the discontinuity of the Riemann problem.

immediately. It is also possible to identify the region containing B. Details on the cases where B is embedded as a sonic line, inside convergent (shock) or divergent (expansion) fans, are reported in Ref. 6. The same procedure is developed at point D (see Fig. 3), at location $N - \frac{1}{2}$, solving the Riemann problem defined with points N and $N-1$.

The numerical procedure just described is conservative but has only first-order accuracy. To analyze the complexities of supersonic conical corner flows, a second-order accurate scheme must be used, at least. The one applied in the present paper has been constructed following the guidelines of the ENO schemes for shock-capturing techniques, originally proposed for time-dependent problems.[7]

The basic ENO theory has many convenient features, particularly the use of piecewise polynomials to obtain an essentially nonoscillatory reconstruction of the solution from its cell averages. In the present case, the definition of the Riemann problem is now founded on suitable values of slopes, related to the initial data, on each cell. The initial data distribution at the abscissa x can be interpreted using piecewise segments with such slope values generating one discontinuity at the interface, $N + \frac{1}{2}$, as shown in Fig. 6. The new distribution of the dependent variables $U = (P, \sigma, h)^T$ in each cell $(y_{N-\frac{1}{2}}, y_{N+\frac{1}{2}})$ is given by

$$U = U_N + s_N(y - y_N)$$

where the vector slope s_N is chosen in the ENO fashion to avoid spurious oscillation at flow discontinuities. If the second order of accuracy is limited to the interpretation of the initial data along y, the discontinuity originating the Riemann problem is defined by the values

$$(U_{N+\frac{1}{2}})'_L = U_N + s_N\,(\Delta y/2)$$

$$(U_{N+\frac{1}{2}})'_R = U_{N+1} - s_{N+1}\,(\Delta y/2)$$

Second-order accuracy in the hyperbolic space-marching direction x is obtained by using the quasilinear form of the motion equations, Eqs. (6), written as

$$U_x + AU_y = 0$$

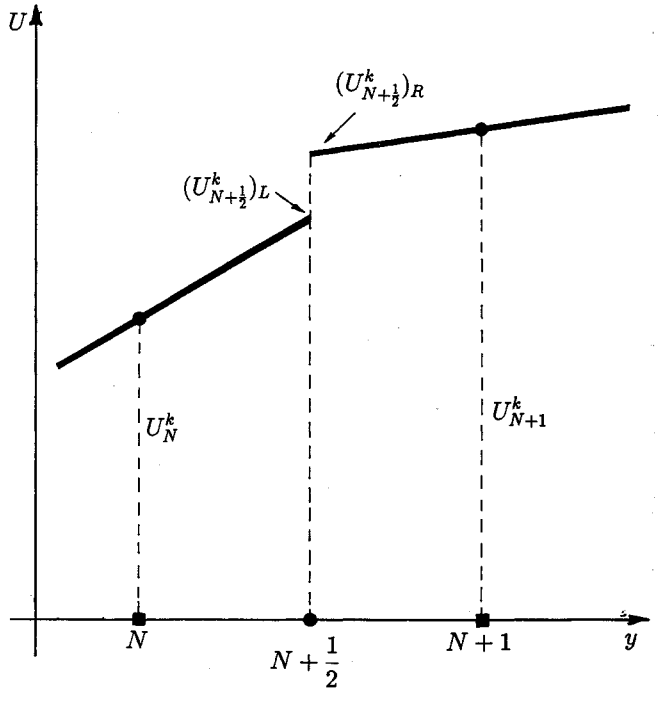

Fig. 6 Initial data interpretation.

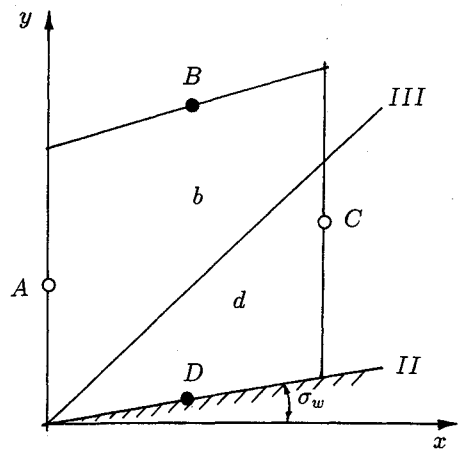

Fig. 7 Finite volume at the wall.

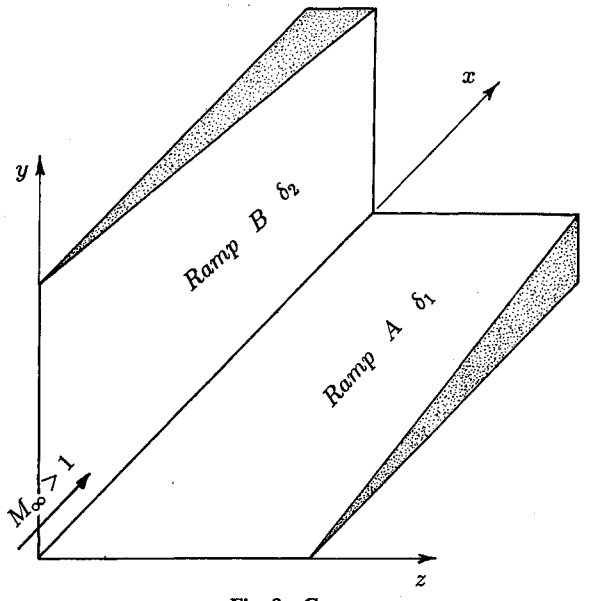

Fig. 8 Corner.

where A is the coefficient matrix of system (6). Therefore, the final values for defining the Riemann problem are provided by

$$(U_{N+\frac{1}{2}})_L = (U_{N+\frac{1}{2}})'_L - A_N s_N\,\Delta x$$

$$(U_{N+\frac{1}{2}})_R = (U_{N+\frac{1}{2}})'_R - A_{N+1} s_{N+1} \Delta x$$

The resolution of the Riemann problem generated by this discontinuity follows the same procedure outlined earlier.

Boundary Conditions

In the present study the boundaries are rigid walls. The volume at the boundary is lying on the wall, as shown in Fig. 7. Let C be the point where the flow is yet unknown, A the initial data point, and D the interface point, respectively. Since there are no volumes below point D, the Riemann problem cannot be defined as at the interior volumes. Instead, a "half" Riemann problem is defined, by assuming the flow in region b determined by point A and making the slope of the streamlines in region d equal to the slope of the wall σ_w. Wave I does not appear, wave II runs along the wall, and only wave III propagates into the flowfield. The values w_D and f_D are computed from flow properties in region d. The latter are obtained by an approximate solution of the half Riemann problem, through wave III:

$$P_d = P_b - \left(\frac{\gamma u^2}{a^2\beta}\right)_b (\sigma_b - \sigma_w)$$

$$\sigma_d = \sigma_w$$

$$h_d = h_b - \left(\frac{p}{\rho}\right)_b (P_b - P_d)$$

Numerical Results

The computational procedure developed earlier has been used to predict and to study the inviscid, supersonic flowfields of conical internal corners generated by two adjacent wedges, as shown in Fig. 8. The conical solution is reached by assuming some initial conditions on the plane (y, z) normal to the coordinate x and carrying out the integration by marching along x. The grid is assumed to develop conically in the space-marching process so that the conical solution will be obtained asymptotically along x, at large distances from the initial plane.

The procedure is conceptually the same used in the time-dependent technique to get steady flow configurations from arbitrarily assumed initial data.

All of the results have been obtained starting with the initial conditions of two-dimensional ramp shocks, generated by the two wedges, where the fluid dynamics fields are two dimensional, and by superimposing the physical variables in the region next to the corner.

Two sets of numerical experiments have been performed. The first one compares the present results with those from Marconi[4] to validate the numerical procedure. The numerical results computed using the present method are shown in Figs. 9–11. Such results refer to two orthogonal ramps, both presenting the angle of 12.2 deg and $M_\infty = 2.47$. The grid in the crossflow plane (y/x and z/x) has 100×100 cells. The upstream flow condition and the geometry of the ramps are the same as in Ref. 4, where the flow has been predicted on the basis of the nonconservative "lambda" formulation and a sophisticated fitting technique of discontinuities. In Fig. 9 pressure contour lines are plotted in the conical coordinates y/x and z/x. This figure shows the five-shock Mach disk configuration. Figure 10 shows the entropy contour lines. Also shown in this figure are the two contact surfaces originating at the interaction of the shocks (triple points) and pointing toward the entropy singularity at the corner line.

The comparison of the present results, given in Figs. 9 and 10, with similar plots reported in Ref. 4 is very satisfactory, and no differences can be found by superimposing the two sets of results. Figure 11 compares the pressure distribution over

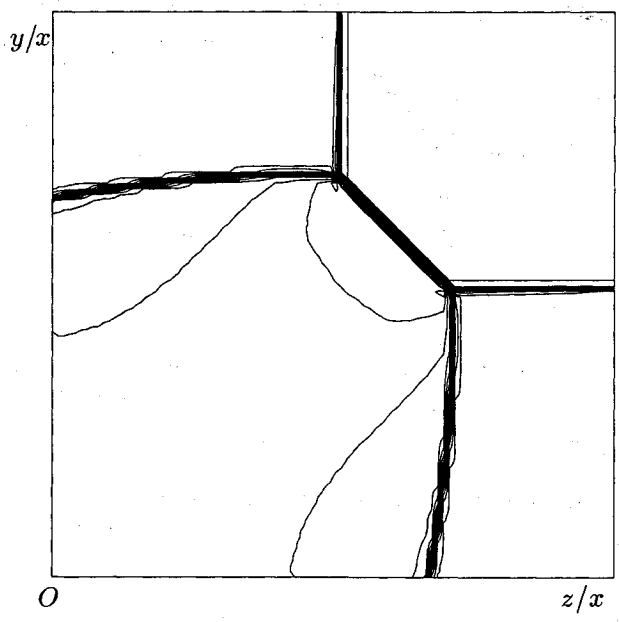

Fig. 9 Corner flow: contour lines of pressure ($\delta_1 = \delta_2 = 12.2$ deg, $M_\infty = 2.47$).

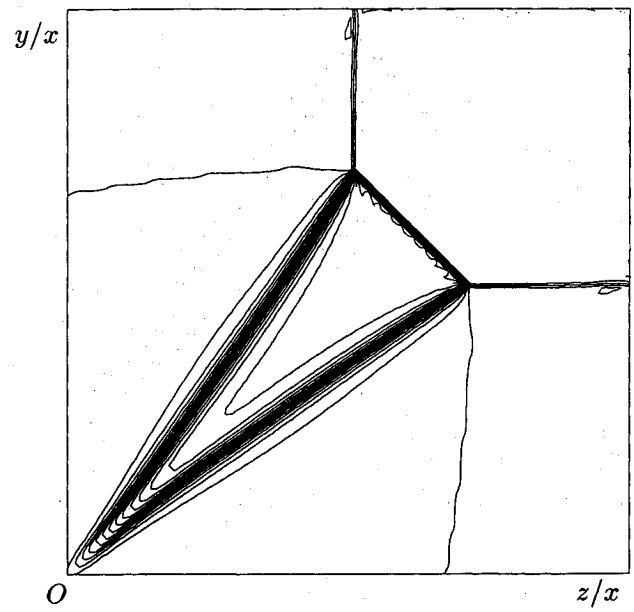

Fig. 10 Corner flow: contour lines of entropy ($\delta_1 = \delta_2 = 12.2$ deg, $M_\infty = 2.47$).

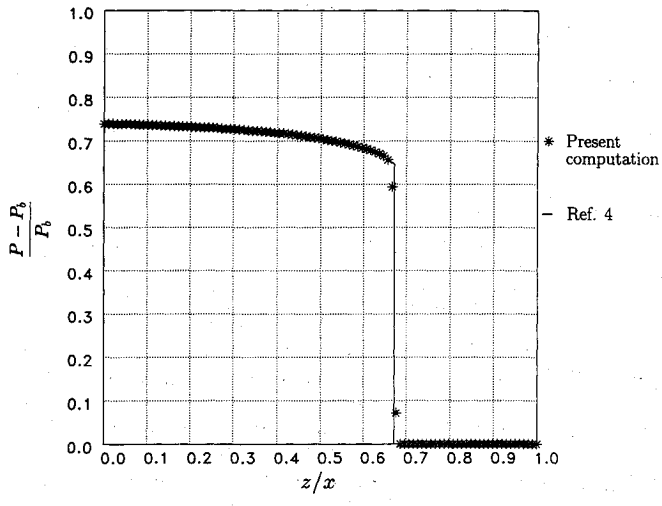

Fig. 11 Comparison with Marconi[4] ($\delta_1 = \delta_2 = 12.2$ deg, $M_\infty = 2.47$).

the wall of one ramp. The ordinate refers to the normalized difference between the local pressure and the values of the two-dimensional ramp (p_B), namely, $(p - p_B)/p_B$. The solid line represents the results from Ref. 4, and the symbols denote the present results.

In the second set of numerical experiments, Mach number and wall geometry effects on the flow pattern have been studied. Figures 12 and 13 show typical crossflow plane entropy contours and crossflow streamlines for solutions generated on a plane grid of 100×100 points at symmetric ramp angles $\delta_1 = \delta_2 = 10$ deg and $M_\infty = 4, 6, 7, 8, 9$, and 10. All such results have been carried out using a full second-order accurate scheme. Figures 12 and 13 at $M_\infty = 4$ show that in that case the two contact surfaces, originated at the triple points, do not produce vortices but point toward the corner line. When the Mach number increases with the same symmetrical geometry, the two contact surfaces originating at the triple points, in the Mach disk configuration, do not point down toward the corner any more. At higher Mach numbers, the shocks (the original two-dimensional shocks and the reflected shock) have very different strengths; consequently, the vorticity concentrated on the contact surfaces is very high, and the contact surfaces tend to roll up, generating two spiral singular-

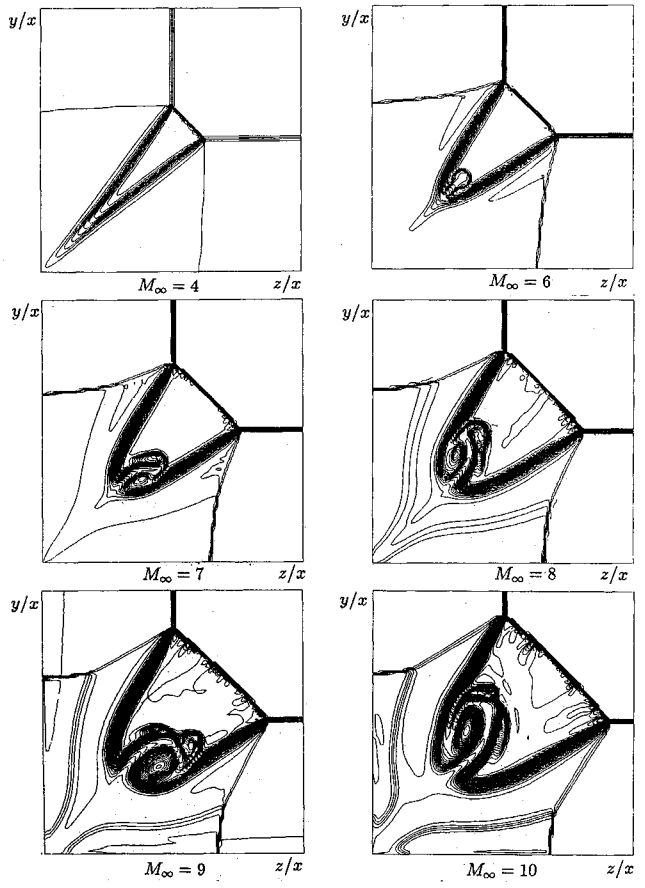

Fig. 12 Computed crossflow entropy patterns at $\delta = 10$ deg for $M_\infty = 4$–10.

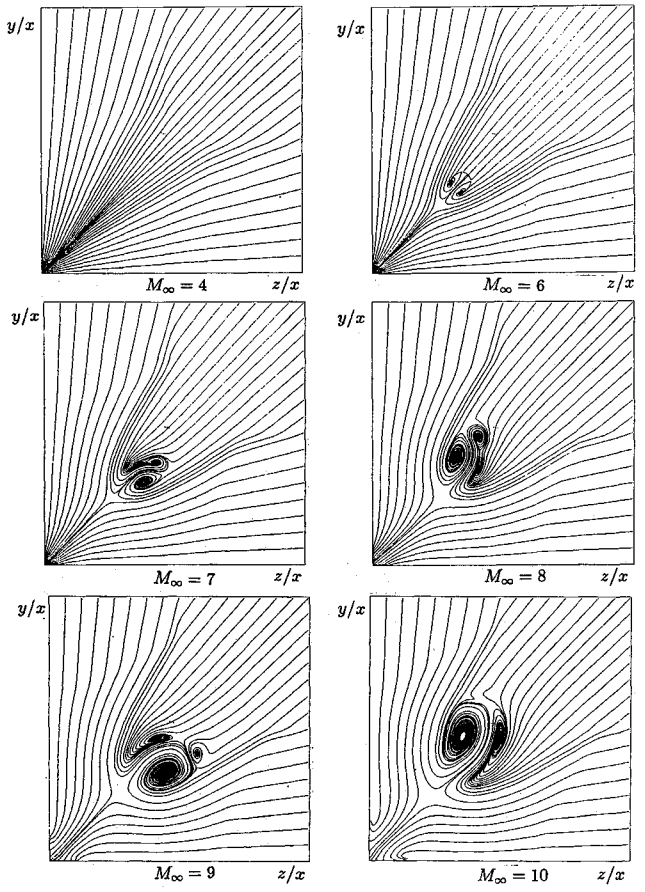

Fig. 13 Computed crossflow streamline patterns for $\delta = 10$ deg for $M_\infty = 4$–10.

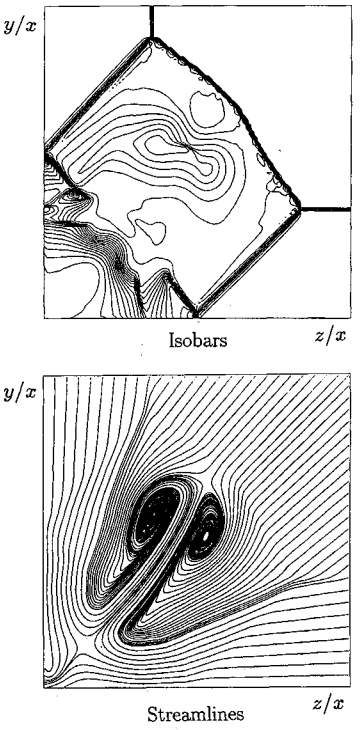

Fig. 14 Interaction between the vortices and shocks ($\delta_1 = \delta_2 = 10$ deg, $M_\infty = 20$).

ities. Such vortices, initially symmetric, are not stable and move to an asymmetric configuration. The asymmetric solution is stable. Two configurations are allowed with the same pattern, where the first is the mirror image of the second with respect to the bisector of the corner. The final numerical solution represents one of these two configurations, depending on the initial data and the round-off error. The phenomenon is remarkable; the vortices affect the slope of the shocks, more vorticity is generated, and new vortices may appear. Such a strong interaction between the vortices and the shocks is shown in Fig. 14 ($M_\infty = 20$ and $\delta_1 = \delta_2 = 10$ deg): the larger vortex, on the left of the figure, changes the slope of the shock forming the Mach stem rather vigorously.

A detailed study of asymmetric solutions appearing on symmetric geometries has been carried out for the case $M_\infty = 10$ using a 50×50 grid.

In symmetric flows (the vortices mirror each other with respect to the bisector of the corner), the pressure distribution on the walls of the wedges should be equal. Any asymmetry of the vortices will be revealed by different pressure forces on the two walls. Therefore, we consider the parameter

$$\Delta F = \frac{1}{2}\frac{F_Y - F_Z}{F_Y + F_Z}$$

where

$$F = \int_0^L p \, dx/L$$

and we plot it in Fig. 15 as a function of the symmetric ramp angle ($\delta = \delta_1 = \delta_2$). At low values of this angle ($\delta \leq 9$ deg), the flow structure looks symmetric, and the value of the parameter is close to zero. At higher angles ($\delta \geq 10$ deg), the flow becomes asymmetric, and the parameter increases monotonically up to an angle ($\delta = 16$ deg) of maximum asymmetry. At more severe ramp deflections ($\delta > 16$ deg), the symmetric pattern is recovered. For ramp angles $\delta \geq 20$ deg, the solution tends to be perfectly symmetrical.

One of the more interesting features of asymmetric solutions discovered here is the complex vortex pattern that

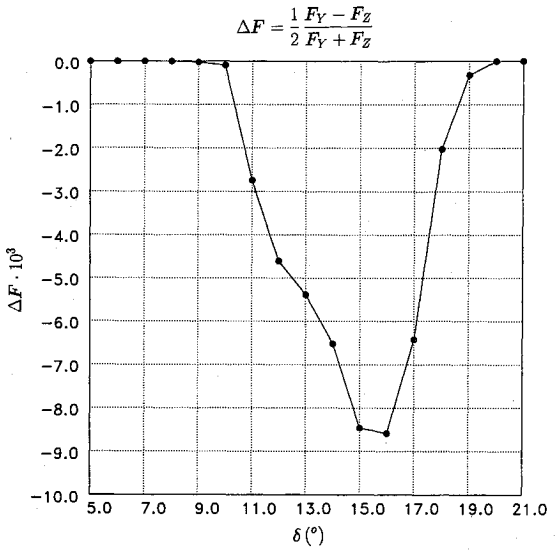

Fig. 15 Computed parameter ΔF at $M_\infty = 10$.

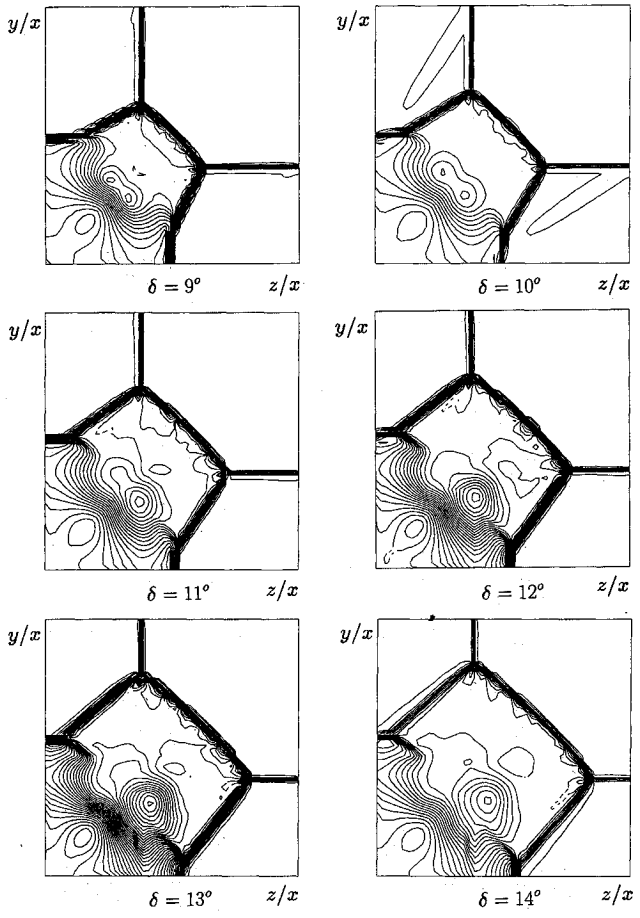

Fig. 16 Computed pressure contour lines at $M_\infty = 10$ for $\delta = 9$–14 deg.

evolves from them. These solutions are illustrated by isobars and streamlines in the crossflow plane of Figs. 16–19. Both pressure and streamline patterns shown in Figs. 16–19 correspond to one point of Fig. 15. Such figures show the evolution of the asymmetric behavior from the $\delta = 9$-deg symmetric solution to $\delta = 20$ deg, through $\delta = 16$ deg where the parameter experiences a peak. At $\delta = 9$ deg, the solution is symmetric. Two vortices occur. The solution is still symmetric at $\delta = 10$ deg with qualitatively similar features, and the vortices become larger and more relevant. At $\delta = 11$ deg, the asymmetric

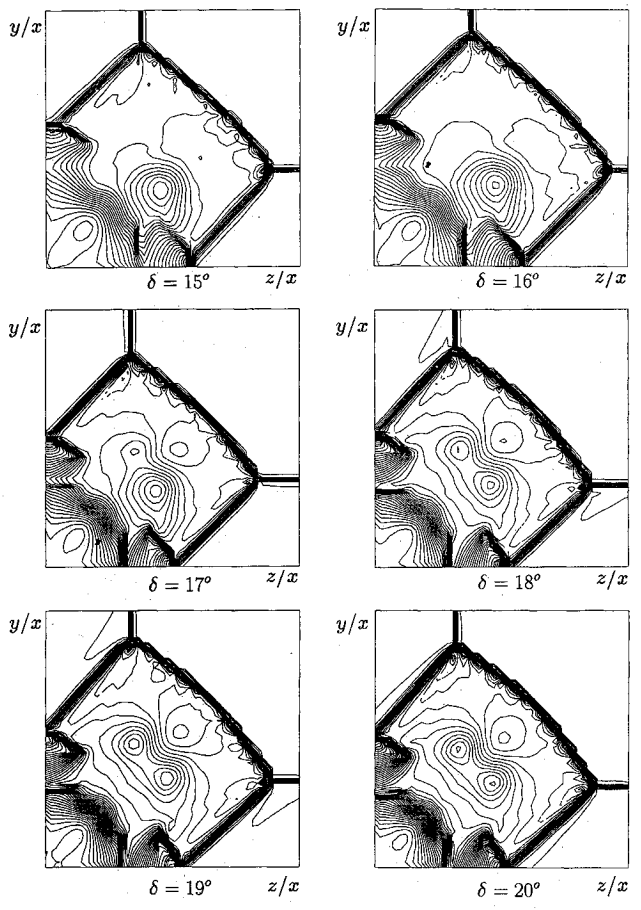

Fig. 17 Computed pressure contour lines at $M_\infty = 10$ for $\delta = 15$–20 deg.

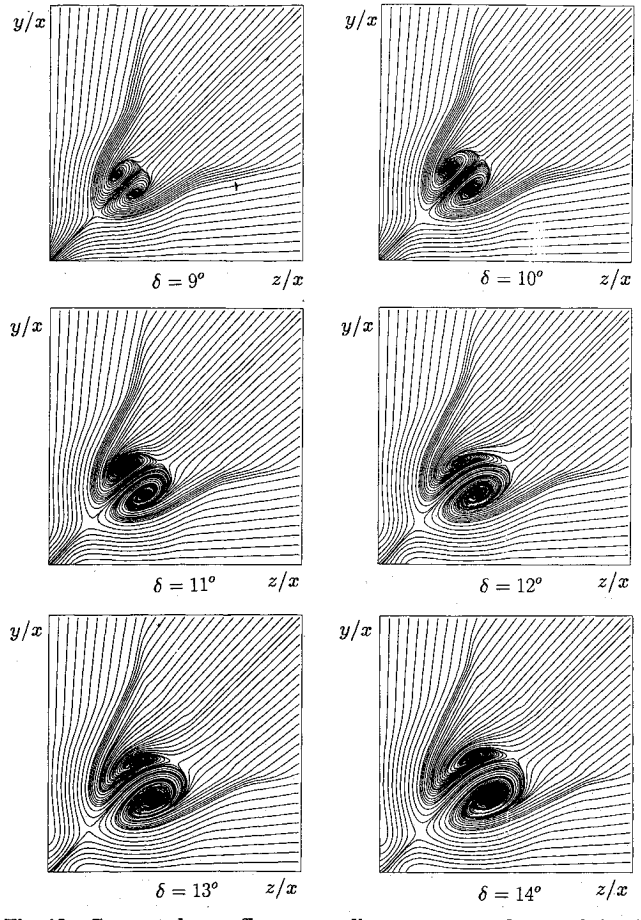

Fig. 18 Computed crossflow streamline patterns at $M_\infty = 10$ for $\delta = 9$–14 deg.

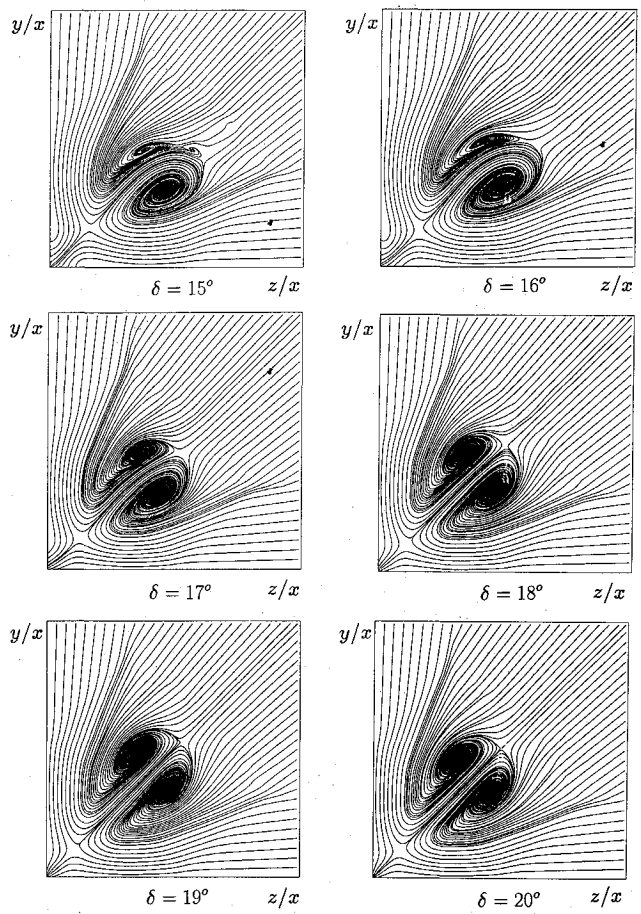

Fig. 19 Computed crossflow streamline patterns at $M_\infty = 10$ for $\delta = 15$–20 deg.

solution appears. The vortices are very large and quite asymmetric at $\delta = 15$–16 deg where the parameter reaches its maximum. Then, at large δ the vortices are still increasing in size, but they will go back to the symmetric solution.

The generation of the asymmetric configuration can be obtained in different ways. In all of the numerical examples, the conical solution begins to be observed as a symmetric one, with a residual (mean square root of the mass flux) monotonically decreasing. If $\delta \leq 9$ deg or ≥ 20 deg, the flow configuration tends to a symmetric pattern and the residual reaches machine zero. In the asymmetric flow range ($10 \leq \delta \leq 19$ deg) the symmetric configuration may move toward the asymmetric one, for different reasons. In some cases the influence of machine round-off error can be strong enough to generate the asymmetric configuration in a relatively small number of integration steps (a few thousands). In other cases, the shifting toward asymmetric flow may occur only after some tens of thousands of steps. To avoid lengthy calculations, it has been found convenient to force asymmetry by artificially generating an asymmetric disturbance on the boundary. Specifically, the upstream conditions have been assumed deflected by 1 deg with respect to the symmetric upstream conditions. This artificial perturbation has been imposed for 50 integration steps. Then, the correct upstream symmetric boundary is restored. If the symmetric flow is stable, the disturbance produces only a temporary oscillation of the conical solution. In those cases where an asymmetric flow is stable, the original symmetric conical solution is permanently shifted (with one or more preliminary oscillations about the bisector line) toward the final stable asymmetric configuration.

An important remark on the influence of numerical viscosity on the solution of asymmetric configurations is in order. Numerical viscosity can indeed modify the range of asymmetry as shown in Fig. 15 ($10 \leq \delta \leq 19$ deg). For instance, in a first-order scheme, the magnitude of the vortices is comparable to those obtained by the second-order scheme, but the numerical viscosity fed into the flow stabilizes the vortices into symmetrical patterns. Also, a rather coarse grid stabilizes the symmetrical vortices because of lack of resolution in describing more complex flow. For instance, the small vortices in Fig. 12 at $M_\infty = 6$ appear more stable the smaller they are relative to the grid size. Also, it should be expected that different schemes affect the range of the asymmetric solutions[8] because of different artificial viscosities of the numerical algorithms.

Another interesting feature of the results shown here is the very similar phenomenology obtained by Siclari and Marconi[9] in the study of supersonic flows on slender cones flying at very high angles of attack. Studying the conical Navier-Stokes solutions on pointed cones at supersonic speed, they showed that two families of solutions exist. One family has a single symmetric solution, and the resulting vortices are symmetric; the second family has two asymmetric solutions (one mirroring the other). The asymmetric solutions exist only at relatively high incidence. However, at larger angles of attack the solutions become once more symmetric. In fact, one diagram in their paper (the side force coefficient on the cone as a function of the incidence) is very similar to Fig. 15. Even if in their study the vortices are produced by viscous effects, the stability seems to be governed by the Eulerian part of the equations of motion. Therefore, the results of Siclari and Marconi[9] can be used to validate our results qualitatively.

Acknowledgments

This work was supported by BRITE EURAM PROJECT AERO 1051/64 Contract AERO-0027-C. The author gratefully expresses his appreciation to M. Pandolfi of the Aerospace Department of the Politecnico di Torino and to F. Marconi of the Grumman Aerospace Corporation for their helpful discussions on various aspects of this work.

References

[1]Wallace, J., and Clarke, J., "Uniformly Valid Second-Order Solution to Supersonic Flow over Cruciform Surfaces," *AIAA Journal,* Vol. 1, No. 1, 1963, pp. 179–185.

[2]Charwat, A. F., and Redekeopp, L. G., "Supersonic Interference Flow Along the Corner of Intersecting Wedges," *AIAA Journal,* Vol. 5, No. 3, 1967, pp. 480–488.

[3]Kutler, P., "Numerical Solution for the Inviscid Supersonic Flow in the Corner Formed by Two Intersecting Wedges," AIAA Paper 73-675, July 1973.

[4]Marconi, F., "Supersonic Inviscid, Conical Corner Flowfields," *AIAA Journal,* Vol. 18, No. 1, 1980, pp. 78–84.

[5]Marsilio, R., and Pandolfi, M., "An Upwind 3D Space-Marching Procedure," *Proceedings of the Third International Conference on Hyperbolic Problems* (Uppsala, Sweden), Vol. 2, July 1990, pp. 715–726.

[6]Pandolfi, M., "Computation of Steady Supersonic Flows by a Flux Difference Splitting Method," *Journal of Computer and Fluids,* Vol. 10, No. 1, 1985, pp. 37–46.

[7]Harten, A., and Osher, S., "Uniformly High-Order Accurate Nonoscillatory Schemes," *SIAM Journal of Numerical Analysis,* Vol. 24, 1987, pp. 279–309.

[8]Marconi, F., private communication, Grumman Aerospace Corp., Bethpage, NY, 1992.

[9]Siclari, M. J., and Marconi, F., "The Computation of Navier Stokes Solutions Exhibiting Asymmetric Vortices," AIAA Paper 89-1817, June 1989.